Evolution of γ′ Particles in Ni-Based Superalloy Weld Joint and Its Effect on Impact Toughness During Long-Term Thermal Exposure

Xian-Kai Fan[1] · Fu-Quan Li[2] · Lei Liu[3] · Hai-Chao Cui[1] · Feng-Gui Lu[1] · Xin-Hua Tang[1]

Abstract

Effects of long-term thermal exposure on γ′ particles evolution and impact toughness in the weld joint of Nimonic 263 (N263) superalloy were deeply studied at 750 °C. Results showed that the precipitates in the weld metal were mainly composed of fine γ′ particles, bulky MC carbides, and small $M_{23}C_6$ carbides. With the thermal exposure time increasing from 0 to 3000 h, γ′ particles in the weld metal grew up from 19.7 nm to 90.1 nm at an extremely slow rate. After being exposed for 1000 h, γ′ particles coarsened and some of them transformed into acicular η phase. At the same time, MC carbides decomposed to form η phase and γ′ particles. This dynamic transition ensured the slight reduction in impact toughness of the weld metal after the thermal exposure, which indicated the stable serving performance of N263 weld joint.

Keywords Ni-based superalloy · Weld joint · Long-term thermal exposure · γ′ Phase evolution · Impact toughness

1 Introduction

The development of advanced ultra-supercritical (A-USC) plant poses great challenges on the physical and mechanical properties of component materials, including high-temperature strength, resistance of oxidation and corrosion, long-term creep stability, fatigue stability, and weldability. The expected service temperature is over 700 °C [1, 2], and ordinary steels can hardly meet these demands. Nimonic 263 (N263) superalloy has been brought into attention as a competitive alternative in recent years [3, 4].

N263 is a precipitation hardening Nickel-based superalloy and is mainly strengthened by γ′ phase $Ni_3(Al, Ti)$. Fine γ′ particles precipitate after solution and aging treatment,

which can present excellent performance for N263 below 750 °C [5]. In order to evaluate the microstructure evolution of N263 after long-term thermal exposure, many studies and researches have been conducted. Zhao et al. [6] substantially studied the transition of phase precipitation up to 900 °C in N263. They characterized the morphology and precipitation behavior of γ′ particles as well as several carbides after different heat treatments and proposed a mechanism of η phase precipitation at the expense of γ′ phase. They also performed thermodynamic calculations to predict the phase stability in this alloy. Kim et al. [7] investigated the formation of $M_{23}C_6$ carbide and η phase, and they performed numerical analysis of γ′ particle coarsening process based on two models in N263 after thermal exposure at 700–870 °C. They also studied the tensile and creep behaviors. Microvoids caused by $M_{23}C_6$ carbides promoted the fracture, while η phase had no significant influence on the crack initiation or growth. Han et al. [8] studied the Portevin–Le Chaterlier (PLC) effect in N263 tensile test up to 760 °C. The PLC effect occurred at low strain rates, and Cr and Mo were responsible for the effect. They also reported that the multi-atomic solute atmospheres in N263 increased locking strength and mean stress drop magnitude. Furthermore, the creep behavior [9] and rupture life [10], high-temperature low-cycle fatigue behavior [11], and intermediate temperature brittleness [12] in N263 have also been studied in the previous literature.

✉ Hai-Chao Cui
  Haichaocui@sjtu.edu.cn

1 Shanghai Key Laboratory of Materials Laser Processing and Modification, School of Materials Science and Engineering, Shanghai Jiao Tong University, Shanghai 200240, China

2 State Key Lab of Advanced Welding and Joining, Harbin Institute of Technology, Harbin 150006, China

3 Shanghai Turbine Plant of Shanghai Electric Power Generation Equipment Co. Ltd, Shanghai 200240, China

It is widely recognized that welding is one of the most important manufacturing methods for its low cost and high efficiency. Although there are lots of papers about Nickel-based superalloy weld joints [13–15], few studies are concerned about the weld joint of N263. Jeon et al. [16] studied the microstructure and tensile properties of N263 weld joint after post-weld heat treatment (PWHT) at room temperature and 780 °C. They reported that the PWHT of solution at 1150 °C for 2 h gave the highest strength values. Kim et al. [17] studied the effects of PWHT on carbides precipitation in N263 gas tungsten arc welding (GTAW) joint. They identified them as Cr–Mo-rich carbides and Ti-rich carbides. They also reported that PWHT increased the tensile strength of N263 weld metal. However, neither of the two studies focused on long-term thermal exposure. In order to ensure the stability of properties serving at high temperature, it is of great significance to investigate and evaluate the microstructure evolution in N263 weld joint during long-term thermal exposure.

In this research, the γ' precipitation and evolution in N263 superalloy weld joint after long-term thermal exposure at 750 °C were systematically analyzed and studied in view of multiple characterization methods. The impact toughness of the weld joint was measured to estimate the stability. This paper effectively evaluated the reliability of N263 weld joint used in A-USC plant during long-term service.

2 Experimental

In this research, the rolled N263 sheet was employed after a two-stage heat treatment: solution treatment at 1150 °C for 1 h and aging treatment at 800 °C for 8 h. The main chemical compositions of materials used in this research are listed in Table 1.

The size of the sheet for welding was 5 mm × 150 mm × 450 mm. There was a half-Y-shaped groove along the 450 mm edge. Butt welding was conducted with an automatic tungsten inert gas (TIG) welding machine. The adopted welding parameters are listed in Table 2. Multilayer welding was conducted from the bottom and then finished up to the top surface. To improve the fluidity of molten metal, the shielding gas was the mixture of 75% Ar and 25% He. The PWHT for an as-welded sheet was performed at 800 °C for 8 h. To investigate the evolution and stability of microstructure, weld joint specimens after PWHT were

Table 2 TIG welding parameters

Current (A)	Voltage (V)	Welding speed (mm/min)	Wire feeding speed (mm/min)
120	11.0–11.2	100	1200

exposed in air at 750 °C due to the requirement of practical operation for advanced ultra-supercritical plants.

Weld joint cross-sectional specimens were cut by wire-electrode cutting and mechanically polished to 1-μm surface finish. To reveal the morphology and distribution of precipitate phases, specimens were chemically etched with Kalling's reagent (2 g $CuCl_2$ + 40 mL HCl + 40 mL C_2H_5OH). Specimens were electrochemically etched with an etchant containing 10 g citric acid, 50 mL HCl, and 250 mL H_2O to observe γ' particles which were small in size and easily etched chemically. To prepare thin foils, small disks of 3 mm in diameter were cut and mechanically thinned to about 50 μm in thickness. Foils were then electrically thinned at − 20 °C at a voltage of 30 V using an electrolyte of 10% perchloric acid and 90% ethanol. Microstructure observation and metallographic characterization were examined by optical microscopy (OM) with Zeiss Imager A2m, scanning electron microscopy (SEM) with JEOL JSM-7800F, and transmission electron microscopy (TEM) with JEOL JEM-2100. Energy-dispersive X-ray spectrometry (EDS) analysis accompanied by SEM and TEM observation was also performed.

The size of base metal and weld metal specimens after long-term thermal exposure for Charpy impact test was 2.5 mm × 10 mm × 55 mm, with a V-notch at the center. The impact toughness tests were carried out at room temperature in air according to the ASTM E23-96 standard.

3 Results and Discussion

3.1 Microstructure Observation of Weld Joint

Figure 1 displays the cross-sectional OM micrographs of the N263 weld joint after PWHT. Due to multilayer welding method from the bottom to top surface, the width of the weld metal ranges from 6.4 mm in the middle to 11.8 mm at the top surface. There is not any evidence of defects such as cracks and pores in the weld joint by preliminary

Table 1 Main chemical compositions of N263 base metal and filler material for welding (wt%)

Elements	C	Cr	Co	Mo	Ti	Al	Ni
Base metal	0.06	20.20	19.80	5.94	2.18	0.48	Bal.
Filler material	0.04–0.08	19.0–21.0	19.0–21.0	5.6–6.1	1.9–2.4	0.3–0.6	Bal.
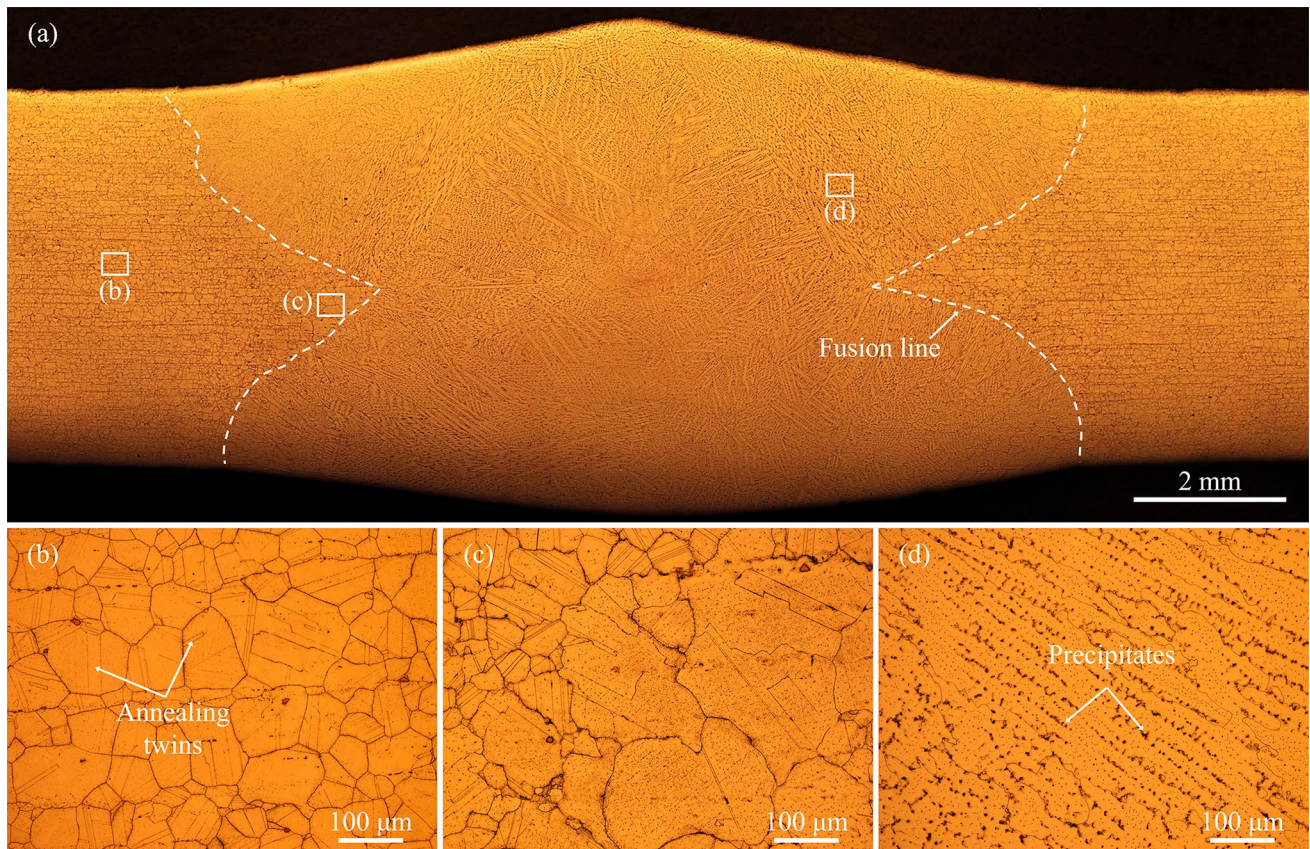
Fig. 1 Cross-sectional OM micrographs of N263 TIG weld joint: macro appearance of weld joint **a**; microstructure of **b** base metal, **c** HAZ, **d** weld metal

observation, indicating the reliable and reasonable weld methods and the appropriate processing parameters.

Figure 1b–d shows the micrographs of different regions in the weld joint, respectively. The base metal (BM) of N263 is composed of γ phase austenite grains with annealing twins. Austenite grains in the heat-affected zone (HAZ) grow seriously because of weld heat, and small particles appear on the matrix. The width of HAZ is quite narrow and less than 0.5 mm at one side. Columnar grains can be observed in the weld metal (WM). There are plenty of precipitates between dendritic structures.

### 3.2 Characterization of Precipitated Particles in Base Metal

The results of microstructure characterization and analysis of N263 base metal are shown in Fig. 2. Many annealing twins can be found in Fig. 2a. A considerable quantity of precipitated particles can be observed on the matrix. According to EDS results and TEM observation with diffraction spot analysis, these particles can be identified as two kinds of carbides, namely MC and $M_{23}C_6$ carbides.

MC carbides are bulky and large, about 3–8 μm in size, appearing gray or dark when observed by SEM. There are not too many MC carbides on the γ matrix. They mainly precipitate within austenite grains, while a few of them can be found on austenite grain boundaries. EDS analysis results in Fig. 3 show that MC carbides are almost composed of Ti, Mo, and C. Therefore, MC can be expressed as (Ti, Mo)C.

$M_{23}C_6$ carbides are small and nearly distributed on the entire γ matrix. Most of them densely precipitate at grain and twin boundaries, and some of them also appear within austenite grains. Figure 2b displays the TEM bright-field image and the selected area diffraction (SAD) pattern of $M_{23}C_6$ carbides at the austenite grain boundary. Small blocky $M_{23}C_6$ carbides with about 100 nm in size line up along the grain boundary. Both $M_{23}C_6$ carbides and the γ matrix crystallize with FCC lattice, and the lattice parameter of $M_{23}C_6$ carbides is about three times larger than that of γ matrix. The SAD pattern displays the orientation relationship between $M_{23}C_6$ carbides and γ matrix:

$$[011]_{M_{23}C_6} \parallel [011]_\gamma \text{ and } (11\bar{1})_{M_{23}C_6} \parallel (11\bar{1})_\gamma.$$

The selected point spectra in Fig. 2d indicate that $M_{23}C_6$ carbides are rich in Cr and the content of Mo is much
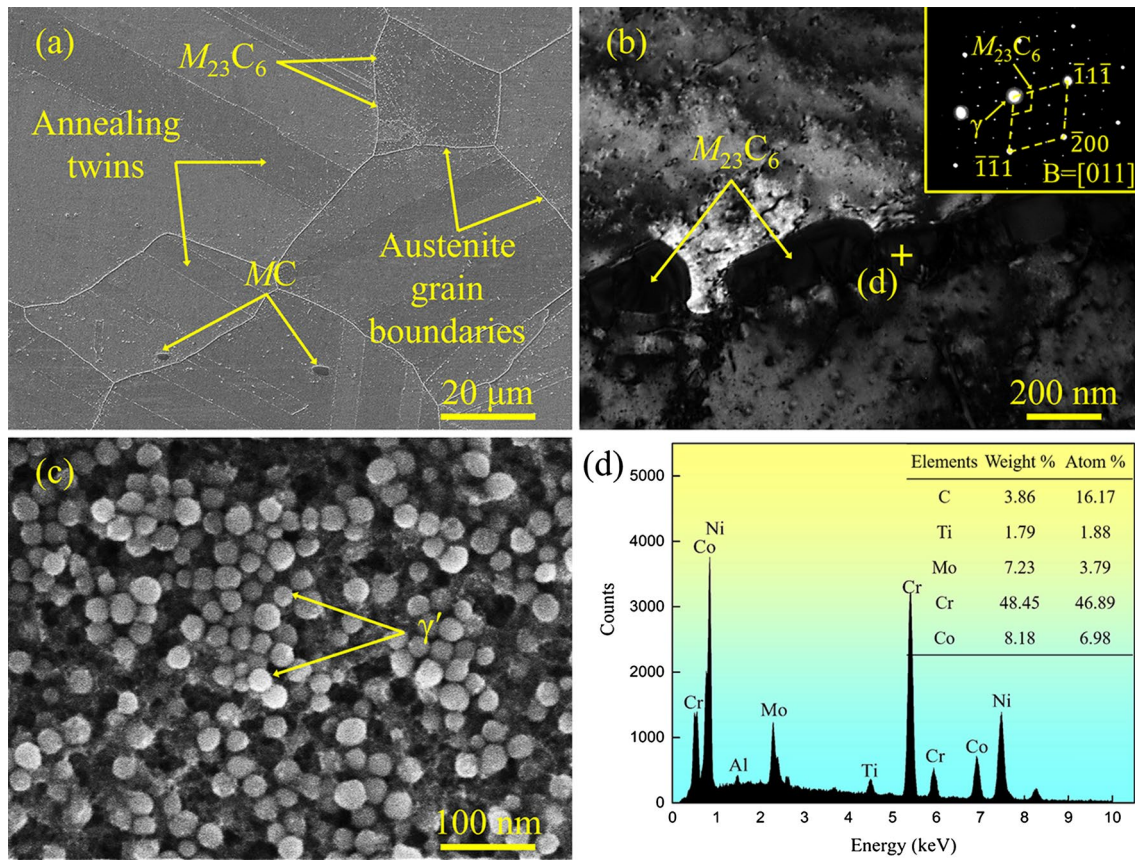
Fig. 2 Microstructure characterizations of N263 base metal: **a** SEM image; **b** TEM image and SAD pattern of $M_{23}C_6$ carbides at the grain boundary; **c** γ' particles in γ matrix; **d** EDS results of $M_{23}C_6$ carbide in **b**
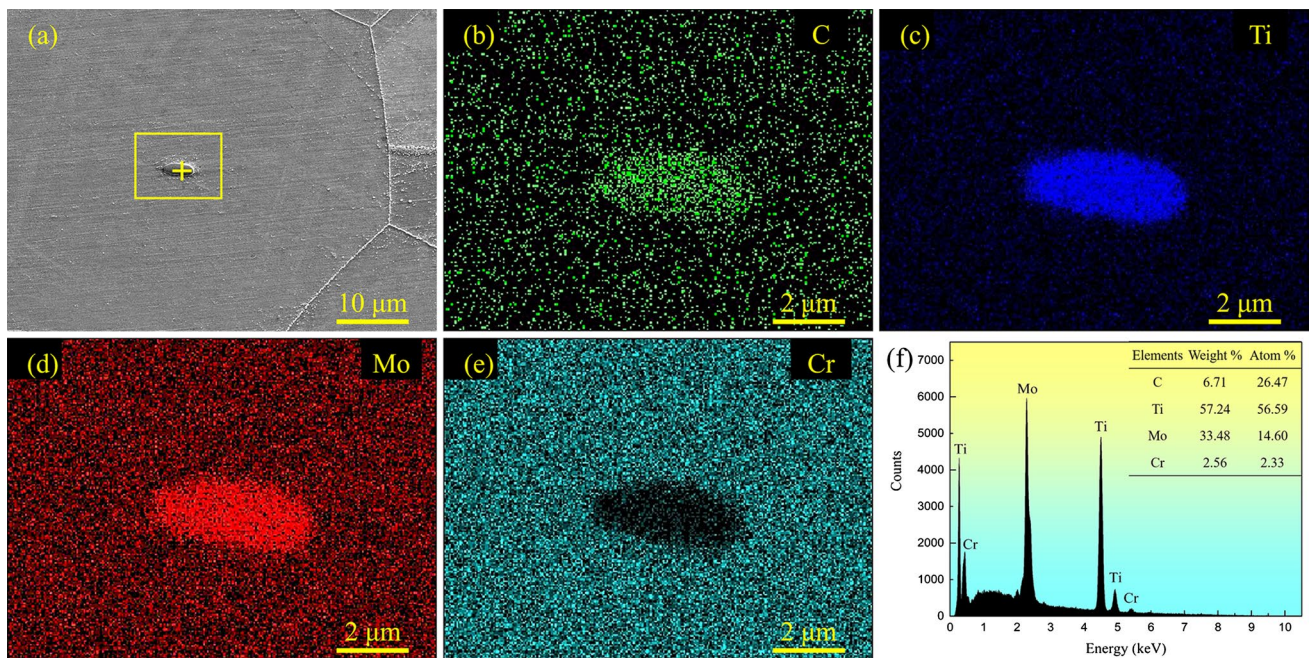

Fig. 3 EDS analysis results of MC carbides in the base metal. MC can be expressed as (Ti, Mo)C

lower. Therefore, $M_{23}C_6$ can be expressed as $Cr_{23}C_6$, which is different from what Kim et al. [17] have identified.

The micrograph of γ′ strengthening phase is shown in Fig. 2c. γ′ particles are fine spherical and densely precipitate all over the γ matrix. The size distribution of γ′ particles is fairly homogenous, and the mean diameter is 23.5 nm. The wide precipitation of fine γ′ strengthening particles in the γ matrix can provide excellent properties for N263.

3.3 Characterization of Precipitated Particles in the Weld Metal

The microstructure characterization of the weld metal after PWHT is shown in Fig. 4. Columnar grains and dendritic structures are observed in the weld metal. Large quantities of precipitates appear at columnar grain boundaries, providing black contrast when observed by OM in Fig. 4a. Figure 4b shows the SEM micrograph of the precipitates. It can
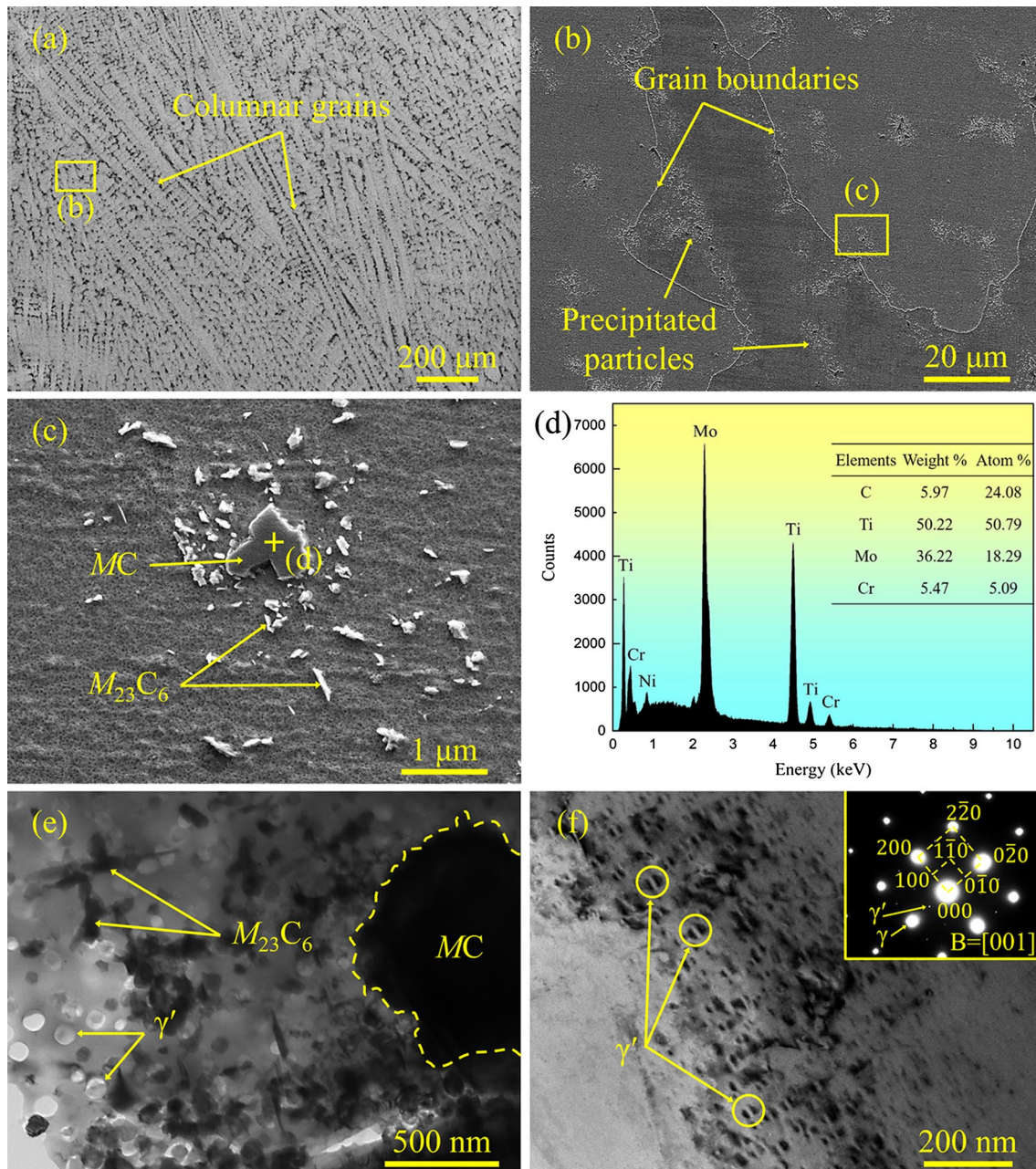
Fig. 4 Microstructure characterizations of the weld metal: **a** dendritic columnar grains; **b** SEM image of precipitated particles; **c** MC and $M_{23}C_6$ carbides; **d** EDS results of MC carbide in **c**; **e** TEM image of precipitated particles; **f** coherent γ′ particles showing strain contrast and lines of no contrast

be clearly found that the precipitates appear as clusters at solidification grain boundaries and between dendritic structures. Nearly, each cluster has plenty of smaller particles, and the microstructure is shown in Fig. 4c. The particles are distinguished as MC and $M_{23}C_6$ carbides with further characterization.

One or several massive and irregular-shaped blocks located at the center are MC carbides. Most of them are 1–5 µm in size, smaller than those in base metal. The selected point spectra of EDS analysis in Fig. 4d indicate that MC carbides in the weld metal are rich in Ti and Mo. This is consistent with MC carbides reported by Zhao et al. [6], but the Mo content in N263 weld metal is much higher.

It is well known that the segregation behavior during solidification can be evaluated by equilibrium partition coefficient of solute elements. The coefficient values of both Ti and Mo are less than 1 in most Nickel-based superalloys [18], which have a strong tendency of gathering to interdendritic regions during solidification. Therefore, MC carbides in the weld metal mainly precipitate between dendritic structures, and the quantity is much larger. The high cooling rate of welding imposes restriction on the subsequently growing process after precipitation, resulting that MC carbides in the weld metal are smaller.

Small in size but large in number particles surrounding MC carbides are $M_{23}C_6$ carbides. They are also found between dendritic structures. After the formation of Ti-Mo-rich MC carbides during solidification, nearby regions become abundant in Cr, promoting the precipitation of $M_{23}C_6$ carbides around MC carbides. Because of the segregation tendency of Cr, $M_{23}C_6$ carbides rarely appear at dendritic cores. Besides, $M_{23}C_6$ carbides in the weld metal are acicular or needle like, different from the blocky ones at grain boundaries in the base metal.

Despite the element segregation and substantial precipitation of MC carbides, γ′ particles can still be observed in the weld metal in Fig. 4e. γ′ particles precipitate as globosity in shape. Although the solidification after welding is rapid, PWHT can provide appropriate conditions for solute elements such as Al in the matrix and remained Ti diffusion, which are main elements composed of γ′ phase. Figure 4f shows the TEM micrograph of γ′ particles in the weld metal. The strain contrast of global coherent γ′ particles and lines of no contrast at the middle of γ′ particles can be clearly observed, indicating the high coherence between γ′ particles and γ matrix in the weld metal. The SAD pattern of γ′ particles presents the orientation relationship with γ matrix:

$$\left[1\bar{1}0\right]_{\gamma'} \parallel \left[1\bar{1}0\right]_{\gamma} \text{ and } \left(11\bar{1}\right)_{\gamma'} \parallel \left(11\bar{1}\right)_{\gamma}.$$

3.4 γ′ Phase Stability in the Weld Metal During Long-Term Thermal Exposure

3.4.1 γ′ Phase Appearance Evolution and Coarsening Behavior

Since γ′ phase plays an important role in strengthening N263, the evolution of γ′ particles during long-term thermal exposure has to be investigated. The micrographs of γ′ particles in the weld metal after thermal exposure at 750 °C for long time are shown in Fig. 5. When the weld metal has not been exposed at high temperature in Fig. 5a, γ′ particles are almost spherical and the dimensional sizes are relatively uniform. The mean diameter of γ′ particles in the weld metal is 19.7 nm, which is slightly smaller than that of base metal in Fig. 2c. When the thermal exposure time does not exceed 2000 h, the majority of γ′ particles maintain spherical. It can be clearly observed that some spherical γ′ particles transform to be elliptic or cubic after thermal exposure for 3000 h.

Figure 5 also displays the coarsening behavior of γ′ particles in the weld metal during thermal exposure. The particle size increases dramatically and the number per unit area decreases with thermal exposure time. Some γ′ particles in extremely tiny size are observed during the coarsening. Two well-known theories to explain this coarsening behavior are the LSW theory presented by Lifshitz, Slyozov, and Wagner [19, 20] and the trans-interface diffusion-controlled (TIDC) theory presented by Ardell et al. [21, 22].

The LSW theory and TIDC theory describe the coarsening process based on bulk diffusion and trans-interface diffusion of solute elements, respectively, which can be written as the following equation:

$$r_t^n - r_0^n = kt,$$
$$n_{\mathrm{LSW}} = 3, \quad k_{\mathrm{LSW}} = 8\Gamma V_{\mathrm{m}} D C_{\mathrm{m}}/9RT,$$
$$n_{\mathrm{TIDC}} = 2, \quad k_{\mathrm{TIDC}} = 32Dl_{\gamma}/81X_{\mathrm{e}}\delta,$$

where r_t is the mean particle size at time t and r_0 is the mean particle size without thermal exposure. The coarsening constant k_{LSW} depends on interfacial energy Γ, particle molar volume V_{m}, diffusion coefficient D, atomic fraction of particle in equilibrium C_{m}, universal gas constant R, and absolute temperature T. Parameter k_{TIDC} depends on diffusion coefficient D, capillary length l_{γ}, composition difference of precipitate and matrix in equilibrium X_{e}, and width of interface δ.

Figure 6a, b shows the fitting curves of particle size versus thermal exposure time under the two models. For nonspherical γ′ particle, the diameter of a circle which has equal area is used to represent the particle size.

Recently, the model with non-integer temporal exponent, n, has been developed [23] and the fitting results are shown
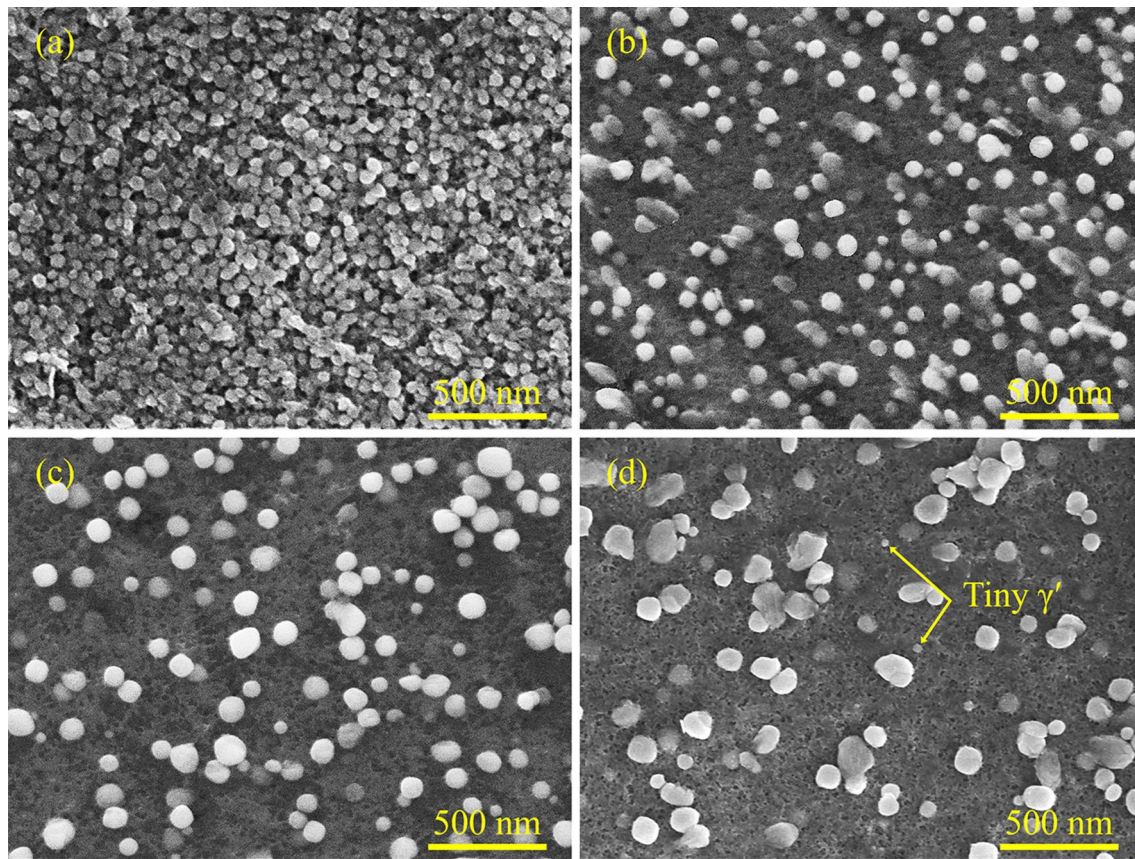
Fig. 5 Morphologies of γ′ particles in the weld metal during thermal exposure at 750 °C for **a** 0 h, **b** 1000 h, **c** 2000 h, **d** 3000 h
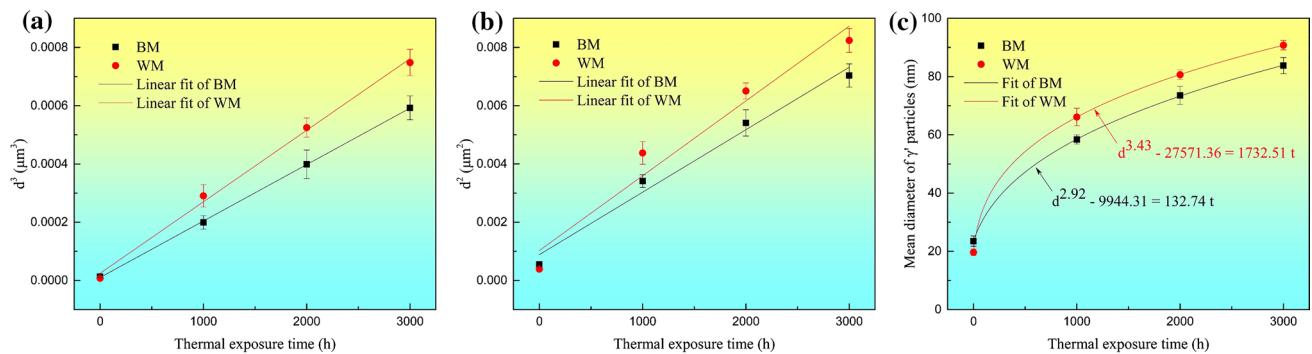

Fig. 6 Curves of γ′ particle size d^3, d^2, and d versus thermal exposure time t under different models: **a** LSW model; **b** TIDC model; **c** non-integer temporal exponent model

in Fig. 6c. As for the weld metal, the temporal exponent, n, is larger than 3, which indicates an extraordinary slow growth rate of γ′ particles and is unusually compared with the former literature [7, 23]. During the thermal exposure, some γ′ particles in the weld metal may transform to η phase while growing and these large ones are eliminated from γ′ size calculation. Besides, MC carbides decomposition can produce γ′ particles in small size. The moderate coarsening

behavior of γ′ particles in the weld metal is beneficial for maintaining the size stability and strengthening effect.

3.4.2 Carbides Transforming to γ′ Particle and η Phase Transformation

During long-term thermal exposure at 750 °C, the microstructure of precipitated particles has changed. Figure 7
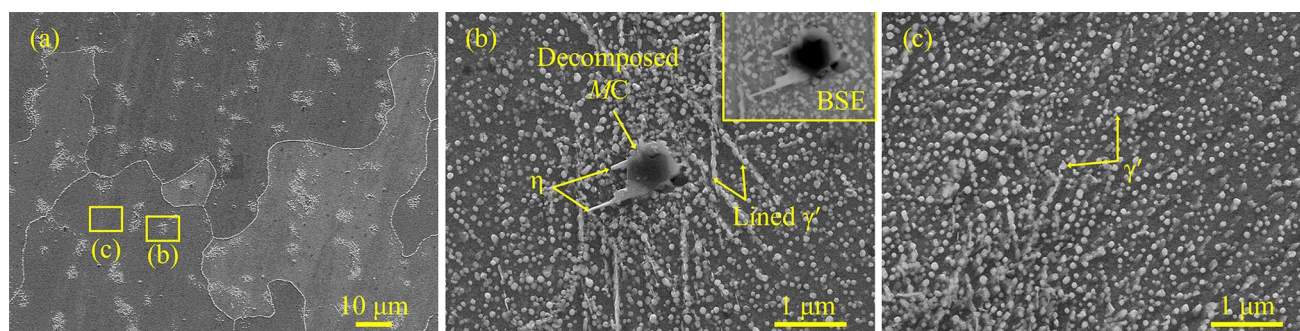
Fig. 7 Microstructure evolution after 1000 h thermal exposure at 750 °C: **a** SEM graphs of interdendritic precipitates in the weld metal; **b** η laths and lined γ' particles are found around the decomposed MC carbide; **c** no η laths appear away from MC carbide

shows the micrographs of evolved precipitates in the weld metal after thermal exposure for 1000 h. The contrast change in Fig. 7b, especially in backscattered electron (BSE) image, indicates the decomposition of MC carbide. Short rod or lath-like phase can be found around MC carbide, which is further characterized as η phase. What should be noticed is that η phase only appears near MC carbide and is hardly found afar, suggesting that the precipitation of η phase has close connection with MC carbides decomposition. Figure 8 shows the characterization of a decomposed large MC carbide in the weld metal after exposure for 3000 h. The BSE image and EDS elemental maps show that the interior part in dark contrast is the

remained Ti–Mo-rich MC carbide, and the surrounding region in light white contrast is rich in Cr.

The behavior of primary MC carbides decomposition in N263 can be described from the perspective of element diffusion with two reactions when exposed at 750 °C. One reaction $MC + \gamma \rightarrow M_{23}C_6 + \gamma'$ is quite classic: MC carbides decompose and act as the source of Ti and C reacting with Ni, Al, and Cr provided by the γ matrix and then generate $M_{23}C_6$ carbides and γ' particles. The precipitation of γ' particles on the remained MC carbide in Fig. 8 validates the reaction commendably. With the generation and accumulation of $M_{23}C_6$ carbides and γ' phase, the diffusion and exchange of solute elements become difficult.
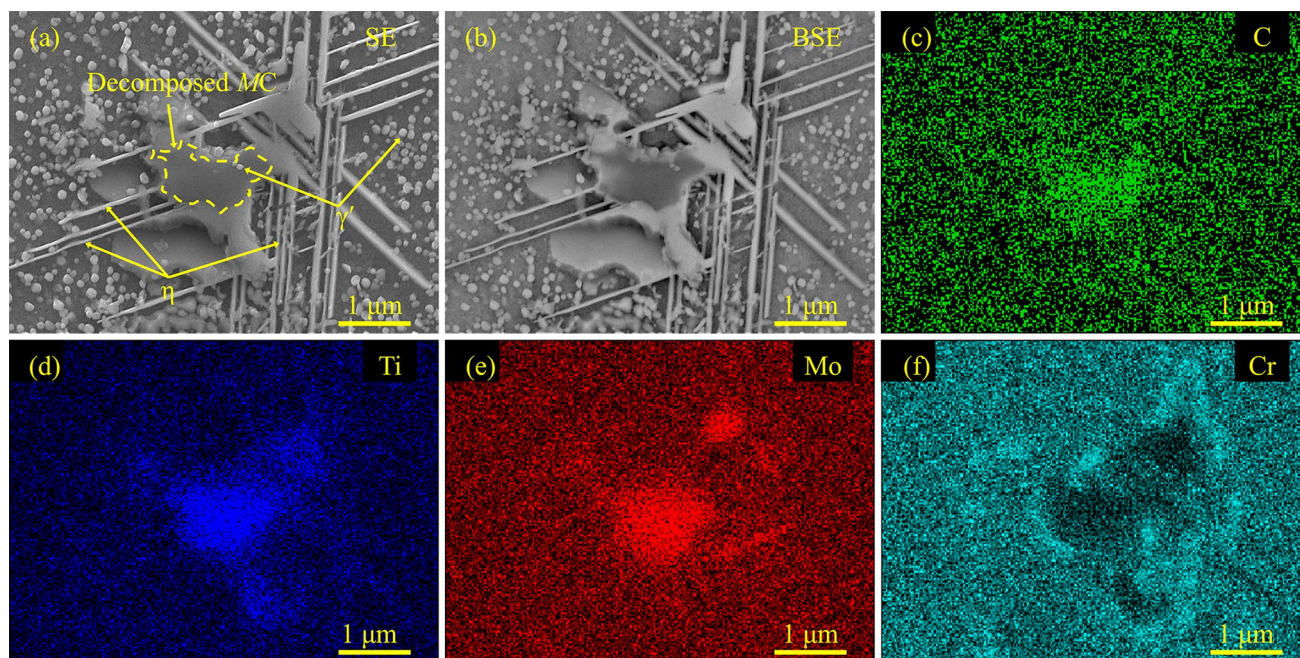

Fig. 8 MC carbides decompose after being exposed for 3000 h and transform to γ' particles and η laths. **a** SE and **b** BSE images showing the small γ' particles on the MC carbide. **c**–**f** EDS elemental maps of C, Ti, Mo, and Cr

Several researches [23–25] have reported that in such system the diffusion of Ni is faster due to its larger diffusion coefficient. As a result, Ni reacts with Ti and promotes the precipitation of η phase, which can be written as $MC + \gamma \rightarrow M_{23}C_6 + \eta$. Based on the above theories, such process in N263 weld metal can be illustrated in Fig. 9.

3.4.3 γ′ Phase Transformation and η Phase Precipitation

In order to investigate and predict the phase evolution and transformation in the weld metal during long-term thermal exposure at 750 °C, thermodynamic calculations have been conducted and the results are shown in Fig. 10. The
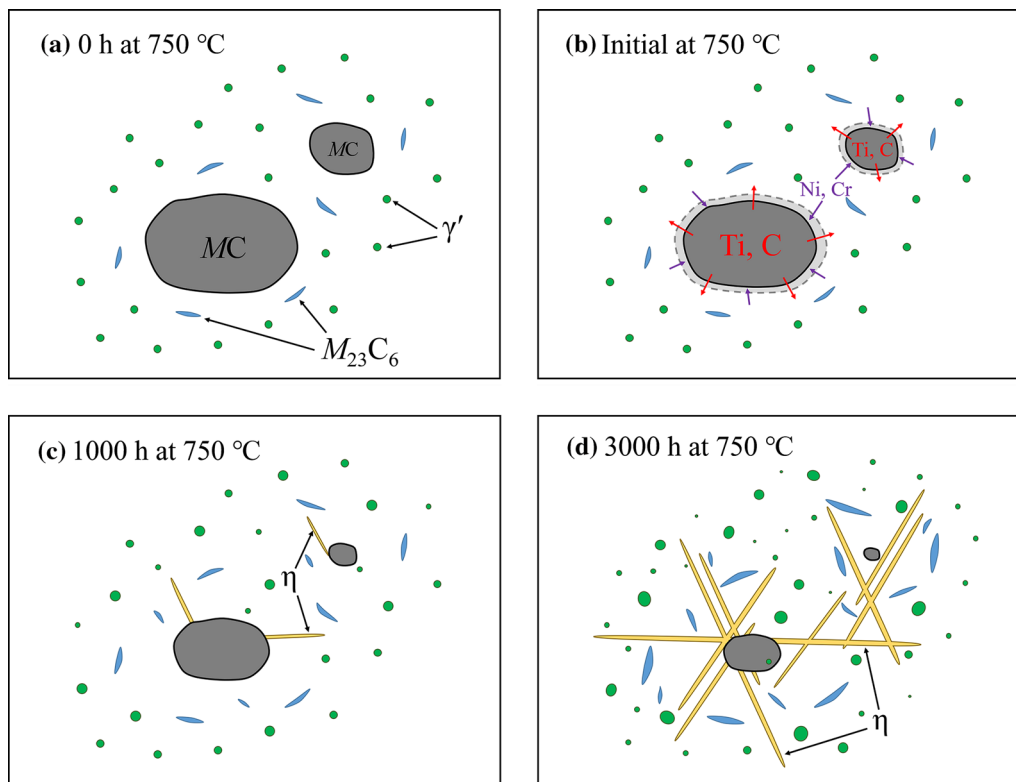
Fig. 9 Schematic illustration of MC carbides decomposition: $MC + \gamma \rightarrow M_{23}C_6 + \gamma' + \eta$
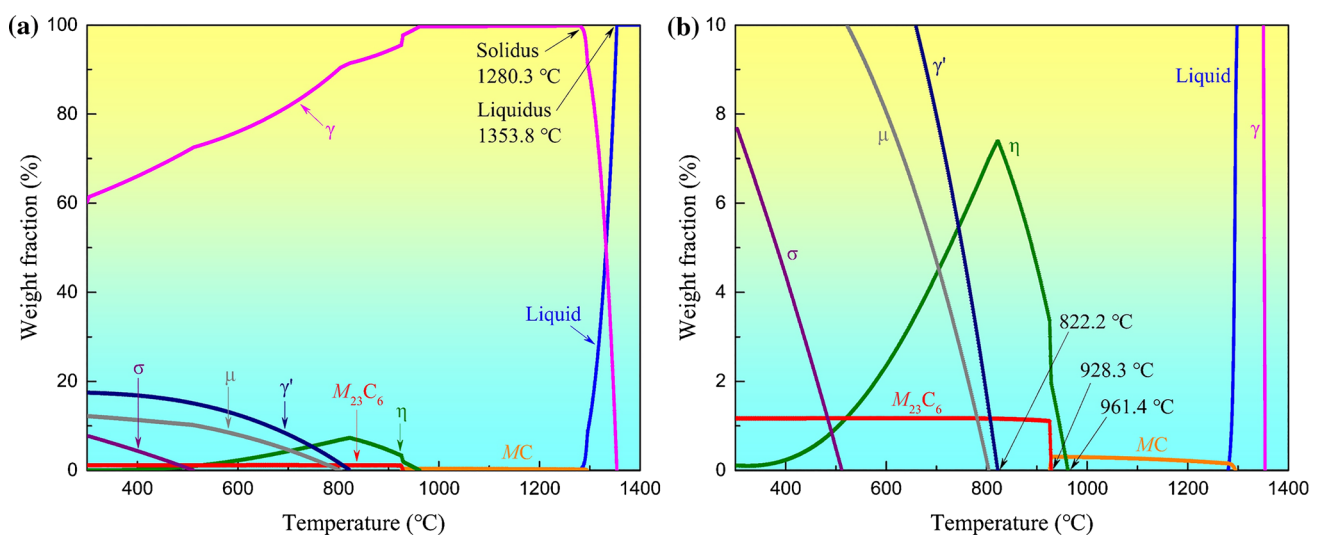
Fig. 10 Equilibrium phase diagrams of N263 through thermodynamic calculation. γ′ phase is metastable and η phase may precipitate during long-term thermal exposure

equilibrium phase diagram indicates that γ' phase is meta-stable at high temperatures. When the thermal exposure time is long enough or the temperature is relatively high, γ' phase may dissolve and η phase will precipitate.

Figure 11 shows the micrographs of η phase in the weld metal after exposure for 3000 h. η phase in the weld metal is mainly found at interdendritic regions and grain boundaries. The chemical composition of η phase is Ni_3Ti, similar to γ' phase. Figure 11a shows that η phase can be etched chemically as well as γ' particles. The morphology of η phase is straight acicular lath or plate. η laths are parallel with the adjacent ones, and the bunches of parallel η laths form a constant angle between each other, displaying a Widmanstatten pattern. According to the TEM characterization in Fig. 11c, η phase has a closely packed hexagonal lattice structure, and the orientation between η phase and γ matrix is as follows:

$$\left[\bar{1}1\bar{1}\right]_\gamma \parallel [0001]_\eta.$$

The precipitation theories of η phase in Ni-based superalloys can be explained in two ways generally. One is that η phase precipitate at the expense of γ' phase. Zhao et al. [6] reported that η phase nucleated at the intrinsic stacking fault in γ' phase and grew to a thin plate at the cost of γ' phase dissolution. Small η plates joined with the others to form long lath. Since the chemical compositions of η and γ' are almost the same, this theory is easy to be understood. The lined γ' particles in Fig. 7b can help demonstrate this theory. Because of the consumption of γ' phase, η laths always precipitate accompanied by γ' free zones, as shown in Fig. 11a.

The other is that η phase precipitates as the decomposition product of MC carbides. The above results about MC carbides decomposition in Figs. 7 and 8 provide proof for this theory. Although it is difficult to find direct evidence that all these η laths precipitate from MC carbides decomposition and are irrelevant with the theory one, the existence of such theory in N263 weld metal is strongly expectable.

3.5 Effect of Long-Term Thermal Exposure on Impact Toughness

Toughness is an important mechanical property to comprehensively evaluate the toughness of the weld metal under the effect of long-term thermal exposure. Figure 12 shows the impact toughness results of base metal and weld metal after being exposed at 750 °C up to 3000 h. With the exposure time increases, the impact toughness values of base metal and weld metal both decrease. Since γ' phase is the main strengthening phase, the impact toughness deteriorates due to the severe coarsening of γ' particles during the thermal exposure. The fracture images show obvious characteristics of brittle rupture along columnar grains, especially in the weld metal after thermal exposure for 3000 h.

Although the impact toughness has a sharp fall when the exposure time is from 1000 to 2000 h, it remains stable and decreases little later. Figure 13 shows the microstructure of the fractured impact specimen in the weld metal after thermal exposure for 3000 h. Features of intergranular rupture can be clearly observed. After thermal exposure for 3000 h, MC carbides located at grain boundaries decompose and η laths precipitate nearby. These precipitates can hinder and deflect the crack propagation, which maintains the stability of impact toughness after thermal exposure for 2000 h. The variation tendency of impact toughness indicates the stable serving performance of N263 weld joint at 750 °C to some extent.

4 Conclusions

1. The precipitates in the weld metal of Nimonic 263 are composed of fine spherical γ' particles, bulky MC carbides, and small $M_{23}C_6$ carbides. γ' particles in the weld metal after PWHT not only distribute densely and homogeneously, but also sustain good coherence with the matrix.
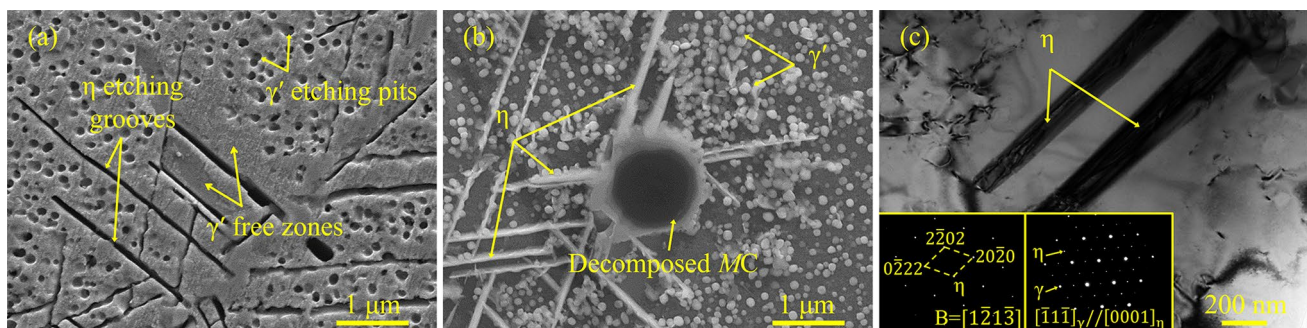
Fig. 11 Characterizations of η phase in the weld metal after being exposed for 3000 h: **a** chemical etching grooves of η phase at the grain boundary and emerged γ' free zones; **b** η phase around a decomposed MC carbide; **c** TEM image and SAD pattern of η phase
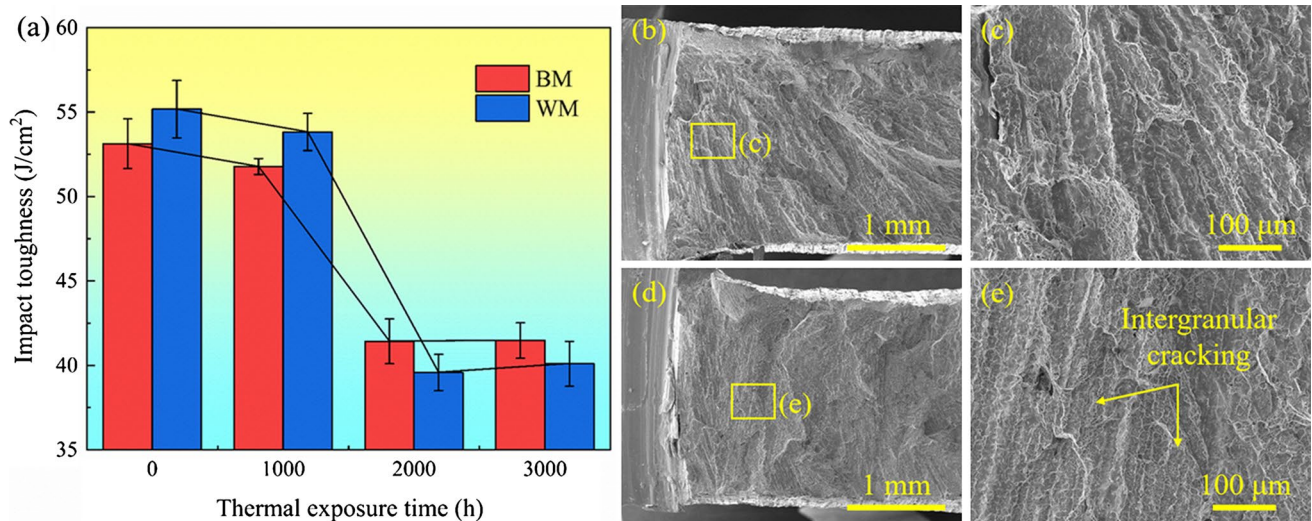
Fig. 12 Impact toughness results of base metal and weld metal after thermal exposure at 750 °C: **a** impact toughness values; **b, c** weld metal fracture without thermal exposure, **d, e** weld metal fracture after thermal exposure for 3000 h
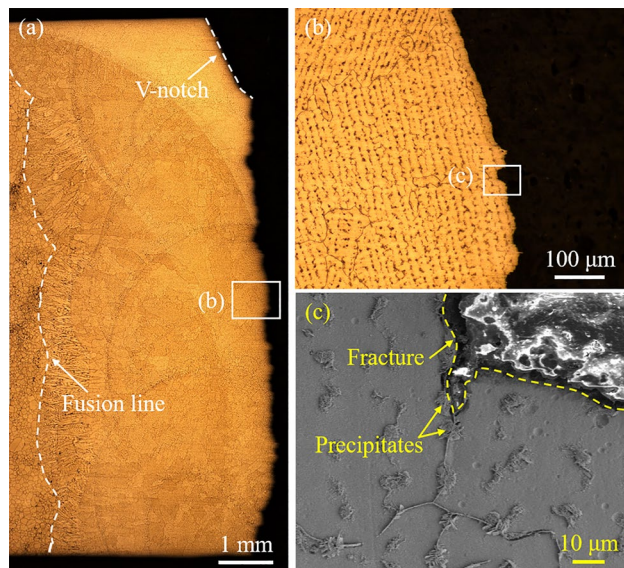
Fig. 13 Microstructures of fractured impact specimen in the weld metal after thermal exposure for 3000 h: **a** the whole fracture; **b** intergranular rupture; **c** precipitates at the grain boundary hinder and deflect the crack propagation

2. With the increase in thermal exposure time, γ′ particles coarsen both in base metal and weld metal, which can be described with a non-integer temporal exponent model. Some γ′ particles transform to η laths, and MC carbides decompose to promote the precipitation of γ′ and η phase.

3. During the thermal exposure, at first, the impact toughness sharply decreases because of the coarsening of γ′ particles. Then, MC carbides decompose and η laths precipitate at the grain boundary, which hinders the crack propagation. Therefore, the impact toughness reduces slightly and tends to be stable later.

References

[1] F. Abe, Engineering **1**, 211 (2015)
[2] S. Guan, C.Y. Cui, Acta Metall. Sin. (Engl. Lett.) **28**, 1083 (2015)
[3] D.L. Klarstrom, L.M. Pike, V.R. Ishwar, Procedia Eng. **55**, 221 (2013)
[4] G. Stein-Brzozowska, D.M. Flórez, J. Maier, G. Scheffknecht, Fuel **108**, 521 (2013)
[5] A. Di Gianfrancesco, *Materials for Ultra-Supercritical and Advanced Ultra-Supercritical Power Plants* (Woodhead Publishing, Sawston, 2017), pp. 571–599
[6] J.C. Zhao, V. Ravikumar, A.M. Beltran, Metall. Mater. Trans. A **32**, 1271 (2001)
[7] I.S. Kim, B.G. Choi, H.U. Hong, J. Do, C.Y. Jo, Mater. Sci. Eng., A **593**, 55 (2014)
[8] G.M. Han, C.G. Tian, C.Y. Cui, Z.Q. Hu, X.F. Sun, Acta Metall. Sin. (Engl. Lett.) **28**, 542 (2015)
[9] A. Manonukul, F. Dunne, D. Knowles, Acta Mater. **50**, 2917 (2002)
[10] S. Bagui, A.K. Ray, J.K. Sahu, N. Parida, J. Swaminathan, M. Tamilselvi, S.L. Mannan, Mater. Sci. Eng., A **566**, 54 (2013)
[11] J.K. Sahu, B. Ravi Kumar, S.K. Das, N. Paulose, S.L. Mannan, Mater. Sci. Eng. A **622**, 131 (2015)
[12] H.J. Chung, J.Y. Huh, W.S. Jung, Mater. Charact. **140**, 9 (2018)
[13] T. Chu, H. Xu, H. Cui, F. Lu, J. Mater. Res. **34**, 2705 (2019)
[14] T.F. Wang, X.J. Di, C.N. Li, J.M. Wang, D.P. Wang, Acta Metall. Sin. (Engl. Lett.) **32**, 1041 (2018)
[15] S.J. Chen, X.X. Ye, D.K.L. Tsang, L. Jiang, C.W. Li, K. Yu, Z.J. Li, Acta Metall. Sin. (Engl. Lett.) **32**, 1032 (2019)

[16] M. Jeon, J.H. Lee, T.K. Woo, S. Kim, Metall. Mater. Trans. A **42**, 974 (2011)

[17] J.K. Kim, H.J. Park, D.N. Shim, Acta Metall. Sin. (Engl. Lett.) **29**, 1 (2016)

[18] J.C. Lippold, S.D. Kiser, J.N. DuPont, *Welding Metallurgy and Weldability of Nickel-Base Alloys* (Wiley, Hoboken, 2011)

[19] I.M. Lifshitz, V.V. Slyozov, J. Phys. Chem. Solids **19**, 35 (1961)

[20] C.Z. Wagner, Z. Elektrochem, Angew. Phys. Chem. **65**, 581 (1961)

[21] A.J. Ardell, V. Ozolins, Nat. Mater. **4**, 309 (2005)

[22] A.J. Ardell, Acta Mater. **61**, 7749 (2013)

[23] A.J. Ardell, J. Mater. Sci. **51**, 6133 (2016)

[24] M. Watanabe, Z. Horita, T. Sano, M. Nemoto, Acta Metall. **42**, 3389 (1994)

[25] K. Fujiwara, Z. Horita, Acta Mater. **50**, 1571 (2002)